Acta Materialia 214 (2021) 116970

Contents lists available at ScienceDirect

Acta Materialia

journal homepage: www.elsevier.com/locate/actamat

Full length article

Fast and accurate lacunarity calculation for large 3D micro-CT datasets

Dániel Sebők[a,*], Lívia Vásárhelyi[a], Imre Szenti[a], Róbert Vajtai[b], Zoltán Kónya[a,c], Ákos Kukovecz[a]

[a] Interdisciplinary Excellence Centre, Department of Applied and Environmental Chemistry, University of Szeged, H-6720, Rerrich Béla tér 1, Szeged, Hungary
[b] Department of Materials Science and Nanoengineering, Rice University, 6100 Main Street, Houston, TX, United States
[c] MTA-SZTE Reaction Kinetics and Surface Chemistry Research Group, H-6720 Szeged Rerrich Béla tér 1, Hungary

ARTICLE INFO

Article history:
Received 23 November 2020
Revised 4 May 2021
Accepted 4 May 2021
Available online 18 May 2021

Keywords:
Lacunarity
Heterogeneity
Microtomography
Materials science
3D image analysis

ABSTRACT

Microcomputed-tomography (micro-CT) is a 3D imaging method capable of revealing the complete inner structure of materials. Besides imaging, micro-CT also provides quantitative information about numerous structural features including lacunarity, which describes the heterogeneity of samples quantitatively. Theoretically, lacunarity is easily calculated using the gliding box method. However, when implemented in 3D, the computational costs of this method increase enormously, thus preventing its widespread use for large micro-CT datasets. Here we suggest a faster alternative method, based on the fixed-grid algorithm, which offers a viable alternative and renders 3D lacunarity calculations on micro-CT data feasible. Since a possible shortcoming of this alternative is that its reduced data could result in an inferior description of the real spatial heterogeneity of the structures, the two methods are compared concerning the accuracy, computational time, and applicability in materials science. The calculations are carried out on real 3D micro-CT datasets. Our implementation of the fixed-grid method can approximate gliding box lacunarity values rapidly and accurately, especially for large datasets of homogeneous structures. Therefore, we propose adding the fixed-grid method lacunarity calculation to the routine micro-CT analysis toolbox. Our image acquisition platform-independent software (Lac3D) to carry out this calculation is made freely accessible here.

1. Introduction

Micro-CT is an important and dynamically spreading characterization tool in materials science [1,2]. While CT (computed tomography) was first introduced as a medical diagnostic tool in the 1970s [3], it soon became a widely used characterization technique in other scientific fields as well. With advancements in technology, high-resolution CTs became available, which are often called micro-CTs due to their ability to provide data with (sub)micron resolution. The technique is based on the different X-ray attenuations of materials, which depends mainly on their chemical composition and density. Micro-CT is a high resolution, non-destructive three-dimensional (3D) imaging technique, suitable for a broad variety of materials [4,5,6]. Its non-destructive nature makes it especially attractive for materials science purposes.

The visualization and investigation of the inner structure of materials is an important task, and while micro-CT can provide valuable 3D images of the internal structure, it is much more than just a visualization tool; a large amount of quantitative data can also be extracted from the measurements, making micro-CT an important diagnostic tool. With this technique, we can harness the full range of spatial information obtainable at the given scale in 3D [7]. It is customary to use micro-CT for porosity determination, and the obtained images could be used to calculate fractal dimension [8,9], which provides information about the complexity of structures [10,11]. Fractal dimension is easily calculated by the box-counting method [12] from micro-CT images even in three dimensions [13,14,15]. Unfortunately, this property is only applicable for self-similar structures, and structures with the same fractal dimension can be highly different from each other in appearance [16]. Other fractal parameters carrying valuable structural information are, for example, second-order fractal metrics such as succolarity, which describes the anisotropy and percolation degree of structures [17], and lacunarity, which describes their heterogeneity and deviation from translational homogeneity [18]. Fractal

* Corresponding author.
E-mail address: sebokd@chem.u-szeged.hu (D. Sebők).

https://doi.org/10.1016/j.actamat.2021.116970

dimension and lacunarity together can describe the complexity and heterogeneity of patterns in one, two, or three dimensions.

Lacunarity (from the Latin "lacuna", meaning gap) was first proposed by Mandelbrot [10] to complement fractal dimension. It can help distinguish between patterns with the same fractal dimensions yet different structures (different in e.g. appearance and heterogeneity); it provides information about texture. It is a multiscale property, insensitive to image borders and independent of the image density. It can describe how space is occupied, provides information regarding the spatial distribution of gaps, and quantifies the degree of translational invariance [18]. Lacunarity is also applicable to real-life datasets with limited – or even no – self-similarity and can be used as a feature for automated image analysis [19] or classification [20]. Calculating lacunarity can be beneficial in various scientific fields from geography [21] and astronomy [22] through food chemistry [23] to neuroscience [24] and oncology [25,26,27]. It can be used to define the heterogeneity of forests from 2D maps [21] and can be a useful property for trabecular bone investigation [28,29] and cell classification [24].

The potential advantages of lacunarity calculations in materials science are not yet widely exploited, but there are several interesting examples where lacunarity calculation added high value to the research. One of the most promising fields is the lacunarity of pores since the spatial distribution of pores in materials can greatly influence their physical properties [30,31]. For example, in the case of building materials (e.g. concrete, brick) an uneven pore distribution can create weak spots and worsen their mechanical strength [32,33,34]. Lacunarity can be used to characterize the heterogeneity of the pore structure of granular materials [35], soil samples [36], oil reservoir rocks [37,38], biomaterials [39] as well as bio-scaffolds [40] and carbon nanostructures [41,42]. Moreover, it can be a valuable structural descriptor in industrial quality control [43,44,45] and also suitable for quantifying the efficiency of mixing [46], a crucial operation in many industries.

The higher the lacunarity, the more heterogeneous the structure and vice versa. However, lacunarity is rarely described as a single numerical value, rather as a function of the box size. A single numerical value – obtained by using a predefined box size –, is only suitable for comparing the heterogeneity of systems, whereas the shape of the lacunarity function provides valuable information about the texture as well. A sudden change in the steepness of the lacunarity curve indicates a change in scale and the point of the change on the abscissa marks the size of the grains/aggregates/clusters/particles involved [47]. The first derivative of the lacunarity curve can be used to identify hidden, scale-dependent patterns in structures more easily [48].

The gliding box method (GBM) is the most frequently used box-counting method to calculate lacunarity [49]. It can also be implemented in 3D by adding one more dimension to the original algorithm [50]. However, calculating gliding box lacunarity for large 3D datasets (e.g. real micro-CT data) is very time-consuming, therefore, there are several attempts to decrease the computational demand [51,52,53]. The fixed-grid method (FGM) [16,54] is a promising alternative. The actual calculation in every individual box is the same as for the gliding box method, however, in FGM the boxes do not overlap, resulting in significantly decreased computational cost. The trade-off is that since lacunarity is a statistical value, less data could mean a less accurate description of the same volume. This concern has kept the fixed-grid algorithm largely out of scientific research, and consequently, the micro-CT community seldom exploits the rich lacunarity information present in each measured dataset.

In this paper, we put forth an easy-to-use, fast calculation method based on the fixed-grid algorithm, which is suitable for lacunarity calculation on huge 3D datasets. The accuracy concern is addressed in detail by comparing the FGM and GBM methods in terms of accuracy, computational time, and applicability to large 3D datasets. First, we prove the operability of our self-developed Lac3D software on 2D datasets, then use the algorithms on real micro-CT data gradually increasing in size. Samples with evident materials science relevance were chosen for this comparison: a sandstone drilling core sample with a relatively homogeneous grain structure and a concrete cube with heterogeneously sized and distributed pores. Having demonstrated the practical equality of the results for large 3D datasets and the computational cost advantage of our fixed-grid algorithm implementation, we finally present exemplary lacunarity calculations for archetypal materials (solid, porous, fibrous, foam-like, and fractured) based on real 3D micro-CT measurements.

2. Materials and methods

2.1. Microcomputed tomography (micro-CT)

Two real-life materials science samples: a sandstone drilling core with quasi-homogeneous phase distribution (Fig. 1.A-C), and a concrete cube ($d < 1$ mm sand grains and EN 197–1 CEM II/B-M (V-LL) 32,5 N cement) with highly heterogeneous pore distribution (Fig. 1.D-F) provided the micro-CT data for the model calculations.

The microtomography measurements were carried out using a Bruker Skyscan 2211 X-ray nanotomograph. The drilling core sample was scanned using an open type pumped X-ray source operating at 180 kV tube voltage and 70 μA emission current (0.5 mm Cu filter). The pixel resolution was 9 μm using a 3 Mp cooled Flat Panel camera with an exposure time of 65 ms. A total of 1201 projection images were obtained by a 360° rotation of the sample with a 0.3° rotation step in 30 min scan time. These values for the concrete cube samples were 130 kV tube voltage, 155 μA emission current (0.5 mm Ti filter), 30 μm pixel resolution, 50 ms exposure time, 1042 projections, 180° rotation, 0.2° rotation step, 30 min scan time. The images were reconstructed with NRecon (Skyscan Bruker, Belgium) software; this step includes the correction of the most common imaging artifacts (i.e. ring artifact, beam-hardening and misalignment). After reconstruction, the volume-rendered 3D CT images were visualized using the CTVox (Skyscan Bruker, Belgium) software. The segmented 3D datasets for the chosen volume of interests (VOIs) were generated by the CTAn (Skyscan, Bruker, Belgium) software after noise reduction on the original images. The same imaging and post processing steps were applied for several archetypal materials science examples; the pixel resolution for the limestone, timber, mortar, Al foam and andesite rock samples were 8, 0.8, 30, 5 and 25 µm, respectively. The lacunarity curves of each sample were calculated for the segmented images by a self-developed software.

2.2. Gliding box method (GBM)

The gliding box algorithm for 2D datasets was published by Allain and Cloitre in 1991 [49]. Fig. 2 shows the principle of operation of this algorithm. On this schematic illustration, a binarized $\boldsymbol{M}$ x $\boldsymbol{M}$ ($M = 8$) random dataset (containing 64 pixels) is represented, where the colored pixels are the objects (Boolean 1) and the white pixels are empty (Boolean 0). In this example, an $\boldsymbol{\varepsilon}$ x $\boldsymbol{\varepsilon}$ ($\varepsilon = 2$) sized box (framed by a solid blue line) is placed on the grid and the number of objects in this box is counted: 3 of 4 pixels are objects, this number is referred to as the mass of the box. In this particular case, the box mass can vary between 0 and 4 (see Table 1). The box is now moved one row to the Y-direction (dashed blue line) and the box mass is counted again (1 of 4). The number of possible box positions is $N(M,\varepsilon) = (M-\varepsilon+1)^2$ (= 49, here). If the number of boxes with size ε containing P object pixels is $n(P,\varepsilon)$,

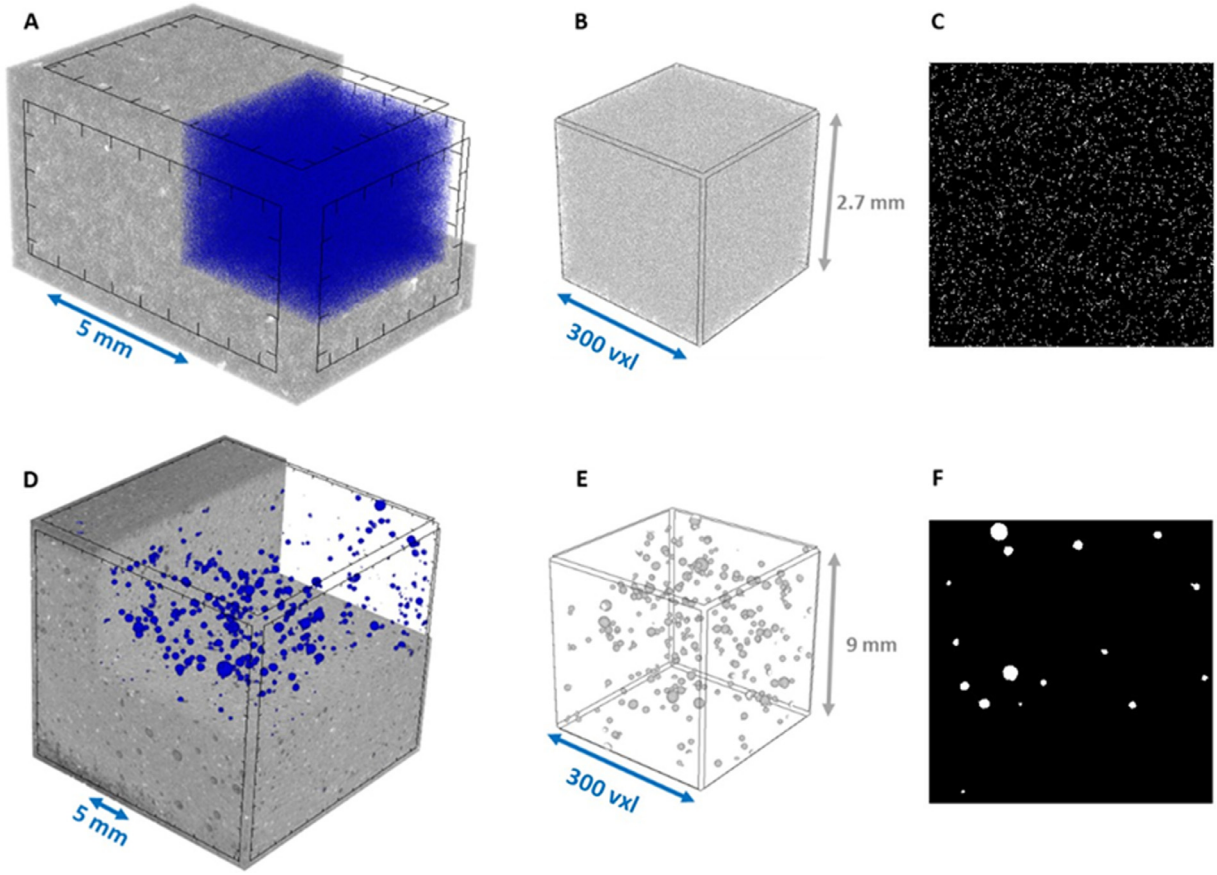

Fig. 1. 3D volume-rendered micro-CT images of (A) a rock core sample (grayscale) with homogeneously distributed sand grain texture (blue) and (D) a concrete cube (grayscale) with a heterogeneous pore structure (blue); (B and E) representative selected volume of interests (VOI) for the calculations in the case of rock core and concrete cube samples, respectively: cubiform volumes with an edge length of 300 pixels (300 × 300 × 300 voxels, i.e. 27,000,000 B/W points in 3-dimension). (C and F) Representative segmented slices from the 3D volume of interests. The difference in the length scales (A, D) comes from the different pixel resolution: it was 9 µm in the case of the core sample and 30 µm for the concrete cube. (For interpretation of the references to color in this figure legend, the reader is referred to the web version of this article.)

Table 1
Calculated data (by GBM) for the example shown in Fig. 2: size of the map, $M = 8$; size of the box, $\varepsilon = 2$; the box mass, P can vary between 0 and 4; $n(P,\varepsilon)$ is the number of boxes containing P object pixels; $Q(P,\varepsilon)$ is the probability calculated by Eq (1); $P{\bullet}Q(P,\varepsilon)$ and $P^2{\bullet}Q(P,\varepsilon)$ are the first and second moments, while $Z^{(1)}$ and $Z^{(2)}$ are the sum of the first and second moments, calculated by Eqs. (2) and (3), respectively. $\Lambda(2)$ is the lacunarity of the dataset for box size $\varepsilon = 2$.

P	n(P,ε)	Q(P,ε)	P•Q(P,ε)	P²•Q(P,ε)
0	5	0.102	0	0
1	25	0.510	0.510	0.510
2	16	0.327	0.653	1.306
3	3	0.061	0.184	0.551
4	0	0	0	0
Sum:	**49**	1	$Z^{(1)} = 1.347$	$Z^{(2)} = 2.367$
Lacunarity:			**$\Lambda(2) = 1.305$**	**$Ln(\Lambda) = 0.266$**

then this frequency distribution can be converted into a probability distribution $Q(P,\varepsilon)$, showed by Eq. (1).

$$Q(P,\varepsilon) = \frac{n(P,\varepsilon)}{N(M,\varepsilon)} \tag{1}$$

The first and second moments of this distribution are determined by Eqs. (2) and (3), and $\Lambda(\varepsilon)$, the lacunarity for box size ε is defined by Eq. (4) [55].

$$Z^{(1)} = \sum_{\varepsilon} P\ Q(P,\varepsilon) \tag{2}$$

$$Z^{(2)} = \sum_{\varepsilon} P^2\ Q(P,\varepsilon) \tag{3}$$

$$\Lambda(\varepsilon) = \frac{Z^{(2)}}{\left(Z^{(1)}\right)^2} \tag{4}$$

2.3. Fixed-grid method (FGM)

A promising alternative to the above-described algorithm could be the fixed-grid algorithm presented here, which is similar to the box-counting method for fractal dimension calculations. The box mass is calculated just like in the gliding box method, but in this case, the boxes do not overlap, thus the number of boxes and the computational resource requirements decrease drastically. This is especially important when extending the algorithm to 3D, which is indispensable for the investigation of spatial heterogeneity of real 3D micro-CT datasets. The schematic illustration of the principle of operation and the corresponding pseudo-code for the three-dimensional fixed-grid method is shown in Fig. S1. It is clearly visible that the box-counting part of the algorithm (marked in blue in the pseudo-code in Fig. S1) is not altered significantly; the only modification is the declaration of a third variable which is assigned to the third dimension. The main difference between the two methods is that the statistical analysis is performed based on the masses of the aforementioned non-overlapping boxes (marked in red in the pseudo-code of Fig. S1). This alteration drastically reduces the number of boxes taken into account. For practical rea-

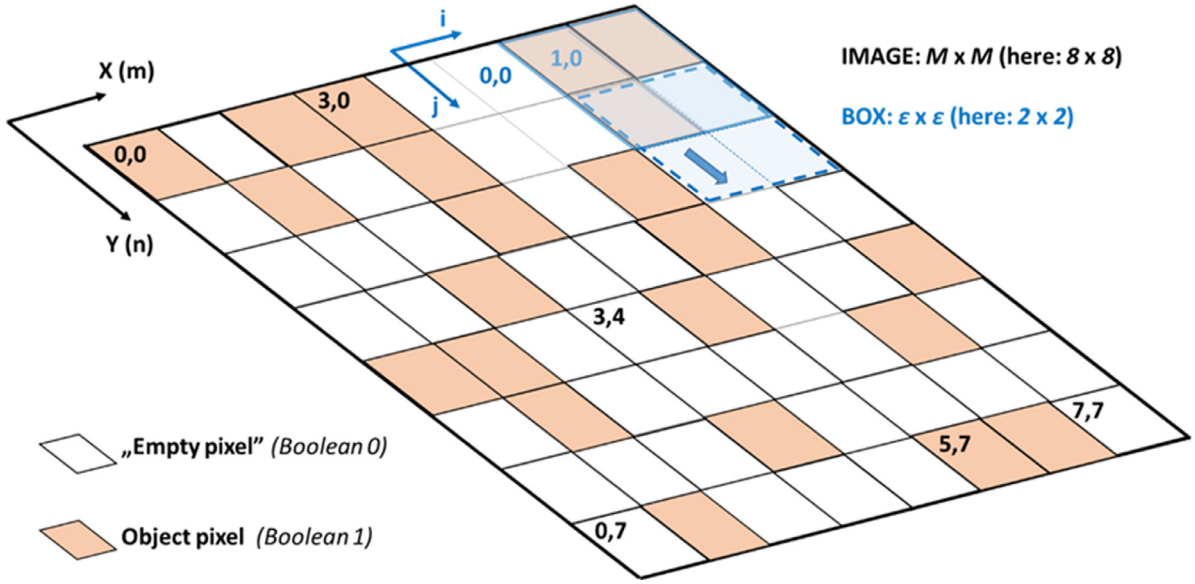

Fig. 2. Schematic representation of the principle of operation of the gliding box algorithm for lacunarity calculation in 2D.

Table 2
Calculated data (by FGM) for the example shown in Fig. 2: size of the map, $M = 8$; size of the box, $\varepsilon = 2$; the box mass, P can vary between 0 and 4; $n(P,\varepsilon)$ is the number of boxes containing P object pixels; $Q(P,\varepsilon)$ is the probability calculated by Eq (1); $P{\bullet}Q(P,\varepsilon)$ and $P^2{\bullet}Q(P,\varepsilon)$ are the first and second moments, while $Z^{(1)}$ and $Z^{(2)}$ are the sum of the first and second moments, calculated by Eqs. (2) and (3), respectively. $\Lambda(2)$ is the lacunarity of the dataset for box size $\varepsilon = 2$.

P	n(P,ε)	Q(P,ε)	P•Q(P,ε)	P²•Q(P,ε)
0	4	0.250	0	0
1	5	0.313	0.313	0.313
2	4	0.250	0.500	1.000
3	3	0.188	0.563	1.688
4	0	0	0	0
Sum:	**16**	1	$Z^{(1)} = 1.375$	$Z^{(2)} = 3$
Lacunarity:			**$\Lambda(2) = 1.587$**	**$Ln(\Lambda) = 0.462$**

sons, only box sizes that are divisors of the size of the volume of interest (VOI) are allowed, thus every voxel is counted at all box sizes. In the example shown in Fig S1., the edge length of the VOI is $M = 8$, which contains 512 voxels. For this VOI the GBM algorithm would use $N(M,\varepsilon) = (M\text{-}\varepsilon+1)^3 = 343$ $\varepsilon = 2$ sized boxes, while this value is only 64 for the FGM. For small datasets the difference in the number of boxes (thus, in the calculation time) is negligible, but for large micro-CT datasets the difference is significant. If $M = 800$ and $\varepsilon = 50$ then the dataset contains 512 million voxels and the masses of 423,564,751 boxes should be counted by the GBM but only 4096 by the FGM. The downside of FGM is that for relatively small datasets the calculated lacunarity values can be inaccurate compared to the results of GBM due to the small number of boxes used. This effect is presented in Table 2: the calculated Λ and $\ln(\Lambda)$ values by the fixed-grid method differ from the data for GBM in Table 1, which is caused by the under-sampling, thus by the different distribution of $n(P,\varepsilon)$ values. For larger datasets, however, the FGM can potentially calculate lacunarity with $R^2 = 0.999$ accuracy (R^2 of the linear curve when plotting GBM datapoints as the function of FGM datapoints) in less than a minute, whereas the same calculation would take days or even weeks by GBM.

Lacunarity was calculated for the model 3D micro-CT datasets both by the gliding box and the fixed-grid methods using a self-developed software (Lac3D), which is developed in an open-source software [56,57]. Results below were all obtained by Lac3D, which is made freely available to the community at http://nanoct.hu/szte/lac3d. The calculations were performed both with a normal performance PC (with Intel® Core™ i3–2348 M @ 2.3 GHz processor) and with a high-performance one (with Intel® Xeon® E5–2640 v4 @ 2.4 GHz processor).

3. Results and discussion

3.1. Comparison of the methods

The 2D verification of Lac3D is provided in the Supplementary section of this article (see Fig. S2). Henceforward, only three-dimensional calculations are described; the accuracy and calculation time of the methods (GBM and FGM) are compared for the real-life examples: two 3D micro-CT datasets, one with quasi-homogeneous phase distribution (Fig. 1. A-C), the other with highly heterogeneous pore structure (Fig. 1. D-F). It has to be noted, that due to the aforementioned restrictions in box sizes for FGM the calculated box sizes do not always coincide for the two methods.

3.1.1. Homogeneous system

Fig. 3. A-C depicts the $\ln(\Lambda)$ vs. $\ln(\varepsilon)$ curves of the homogeneous patterns for $M = 50$, 150, and 300 VOI sizes, respectively. It has to be noted, that the solid lines connecting the data points were added for easier viewing and are not fitted to the data. It can be established that the value of $\ln(\Lambda)$ becomes nearly zero at low $\ln(\varepsilon) = 3.218$ value ($\varepsilon = 25$). Furthermore, this value does not change significantly for bigger VOIs, indicating the homogeneity of the texture. Another important finding is that the results of the traditional GBM and our FGM estimation are in good agreement ($R^2 \geq 0.998$) even for small VOIs.

The calculation times for gradually increasing VOIs are shown in Fig. 3.D. The GBM calculation times for increasing box sizes can be described with a symmetrical bell curve, the maximum of which is when the box size is half of the size of the VOI. Also, the calculation time increases drastically with increasing VOI size. For $M = 150$ the calculation time of the full range is a little over an hour, while if the edge length of the VOI is doubled the total calculation time jumps up to 69 h. Following this trend, the calculation time of even bigger (thus more representative) VOIs would be extremely long, hence the application of this method is not practical for large 3D datasets. This issue will be addressed in the next

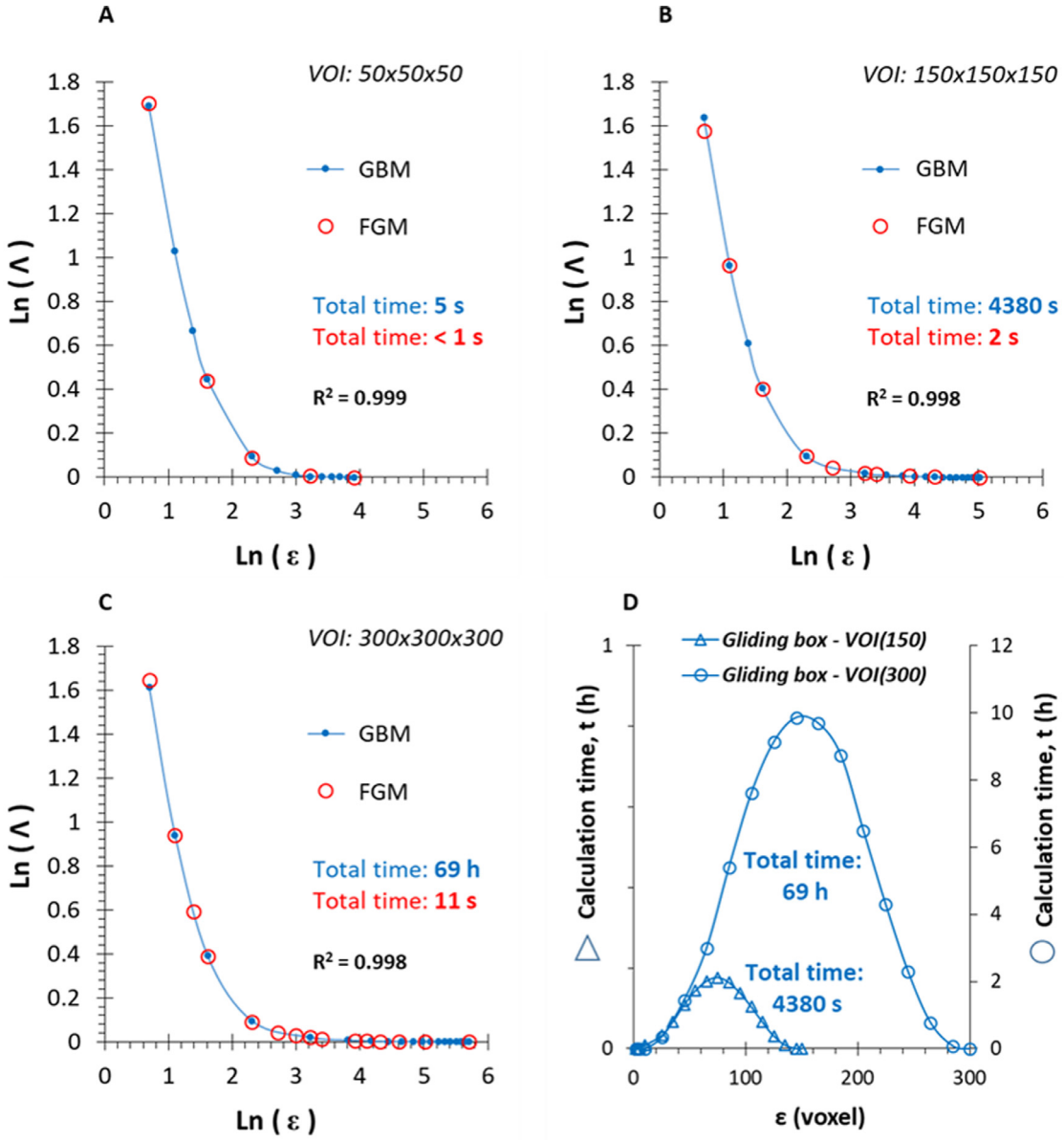

Fig. 3. Ln(Λ) vs. ln (ε) curves for the rock core samples homogeneously distributed sand grain texture at different VOI sizes obtained by gliding box (blue lines with dots) and fixed-grid (red circles) methods: (A) 50 × 50 × 50, (B) 150 × 150 × 150, and (C) 300 × 300 × 300. (D) shows the typical GBM calculation times of each point and the total time corresponding to (B) and (C). Note that FGM calculation times are not shown in part (D) because they are not commensurate with the long timescales of GBM. (For interpretation of the references to color in this figure legend, the reader is referred to the web version of this article.)

section, and the information obtainable from calculations for only a narrower range of box sizes (ε = 2–35 and ε = 2–55) will be discussed.

In conclusion, it was found that the value of lacunarity stabilizes relatively fast, thus the fixed-grid algorithm gives a good approximation of the GBM results for small VOI sizes. For homogeneous textures, the FGM can routinely be used in 3D lacunarity calculations, since it provides reliable data in significantly less time than the gliding box algorithm.

3.1.2. Heterogeneous system

Fig. 4 shows four representative volumes of interests for the calculations in the 3D volume-rendered micro-CT images of the heterogeneous pore structure in a concrete cube. These are cubiform volumes with an edge length of M = 200, 400, 600, and 800 voxels (they represent 8, 64, 216, and 512 million binary points, respectively, in three dimensions). The volume showed in Fig. 4.D indicates the positions of smaller VOIs within the largest one.

The lacunarity curves calculated by GBM and FGM for the M = 50, 100, 200, 300, 400, and 500 voxels sized VOIs can be seen in Fig. 5. The GBM lacunarity curves were only calculated for a smaller range of box sizes (ε = 2–55) in this case, due to the very long computational time (see Fig. 3); the tendency and the accuracy of FGM calculation compared to GBM, however, is obvious even for this limited range. It can be seen in Fig. 5.A-B that there are significant differences in the results of the two methods (R^2 = 0.991) for small VOI sizes (M = 50 and 100). This can be a result of under-sampling, which is mainly problematic for small VOI sizes, and considerably less significant for homogeneous systems, which is in direct relation with the statistical nature of lacunarity (see Tables 1 and 2). However, with increasing M values the accordance of the two methods improves (Fig. 5.C-F). For small VOIs the lacunarity curve cuts off (i.e. $\Lambda \approx 1$) at around $\ln(\varepsilon) = 3.912$ (ε = 50), while for the larger volumes this value is closer to $\ln(\varepsilon) = 5$ (ε = 150), which is more realistic for hetero-

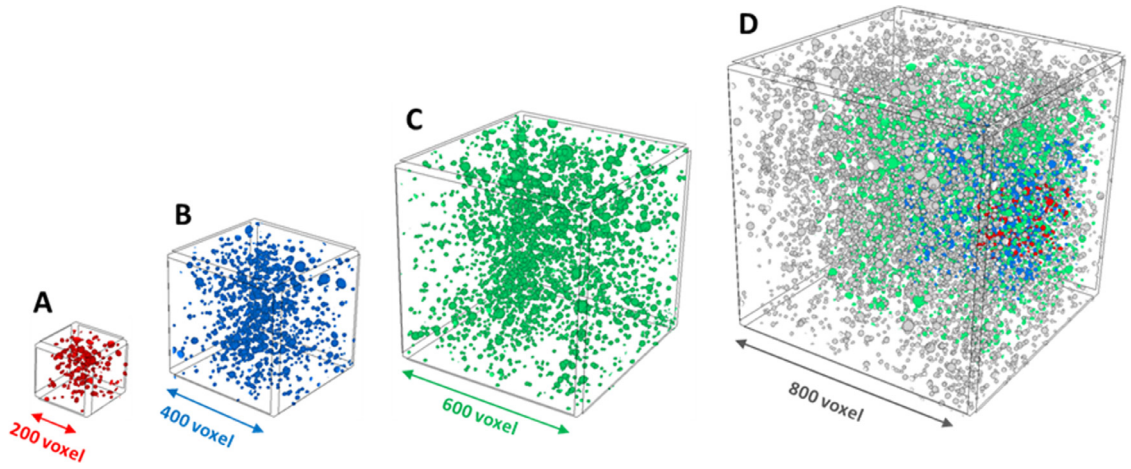

Fig. 4. 3D volume-rendered micro-CT images of the heterogeneous pore structure in the concrete cube; representative selected volume of interests (VOIs) for the calculations: cubiform volumes with an edge length of (A) 200, (B) 400, (C) 600 and (D) 800 voxels (8, 64, 216 and 512 million B/W points, respectively, in 3-dimension). Volume (D) shows the positions of smaller VOIs within the largest one. (For interpretation of the references to color in this figure legend, the reader is referred to the web version of this article.)

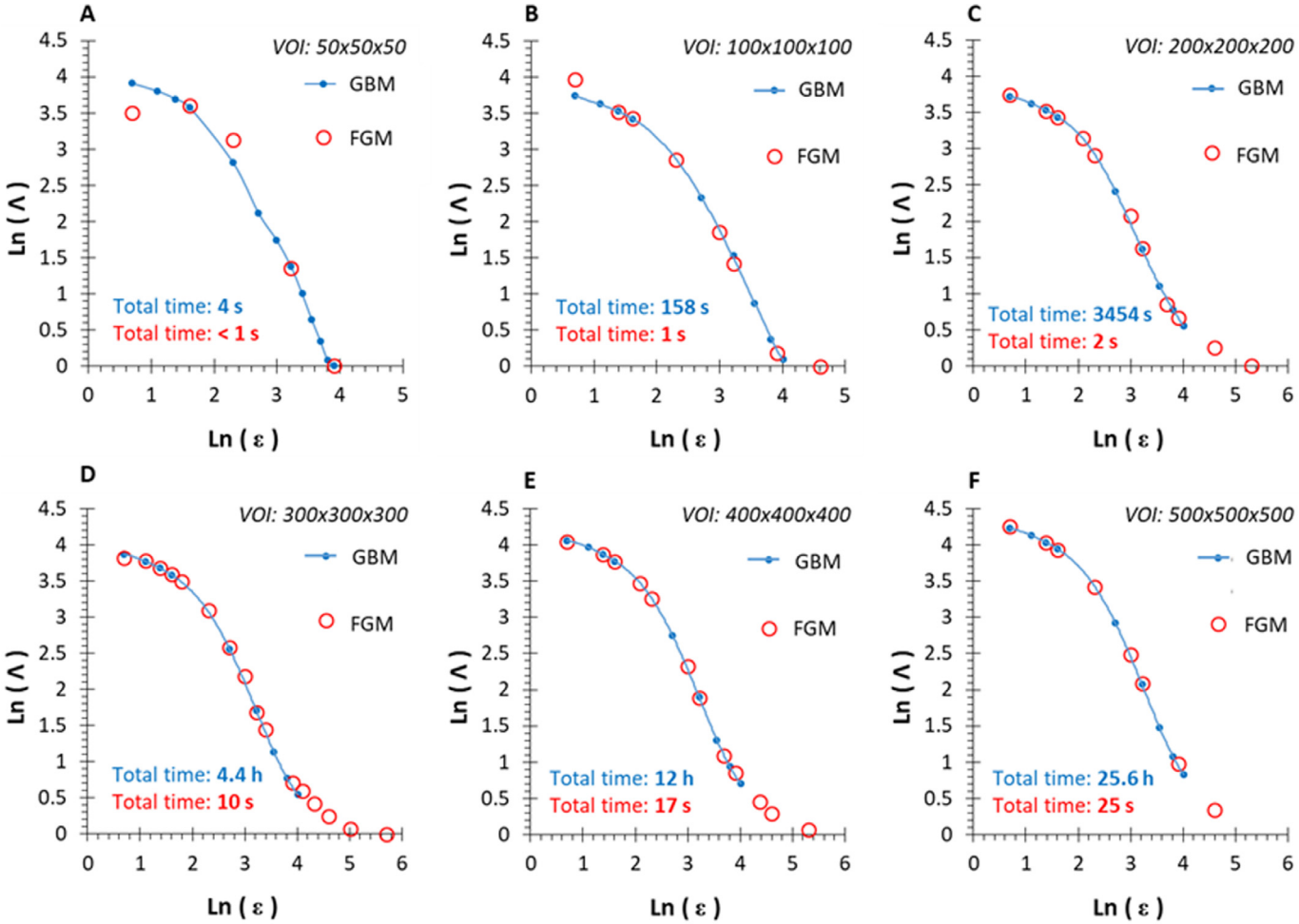

Fig. 5. Ln(Λ) vs. ln (ε) curves for the concrete cube samples heterogeneously distributed pore structure at different VOI sizes obtained by gliding box (blue lines with dots) and fixed-grid (red circles) methods: (A) 50 × 50 × 50, (B) 100 × 100 × 100, (C) 200 × 200 × 200, (D) 300 × 300 × 300, (E) 400 × 400 × 400 and (F) 500 × 500 × 500. The curves are calculated with the gliding box method only for ε = 2, 3, 4, 5, 15, 25, 35, 45 and *55* box size values. (For interpretation of the references to color in this figure legend, the reader is referred to the web version of this article.)

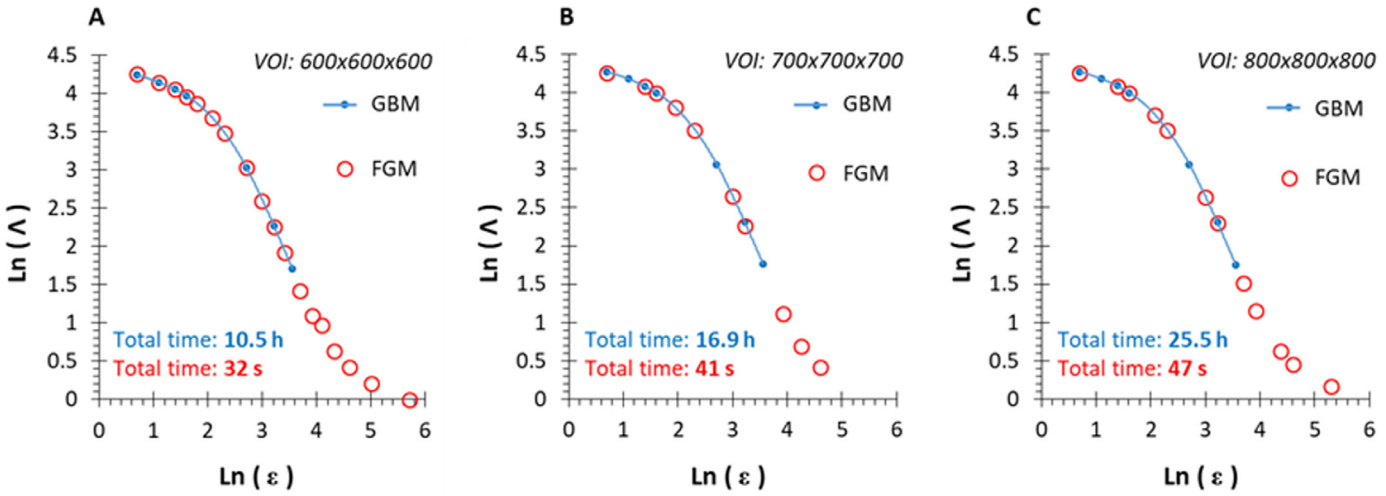

Fig. 6. Ln(Λ) vs. ln (ε) curves for the concrete cube samples heterogeneously distributed pore texture at different VOI sizes obtained by gliding box (blue lines with dots) and fixed-grid (red circles) methods: (A) 600 × 600 × 600, (B) 700 × 700 × 700, (C) 800 × 800 × 800. The curves are calculated with the gliding box method only for ε = 2, 3, 4, 5, 15, 25, and *35* box size values. (For interpretation of the references to color in this figure legend, the reader is referred to the web version of this article.)

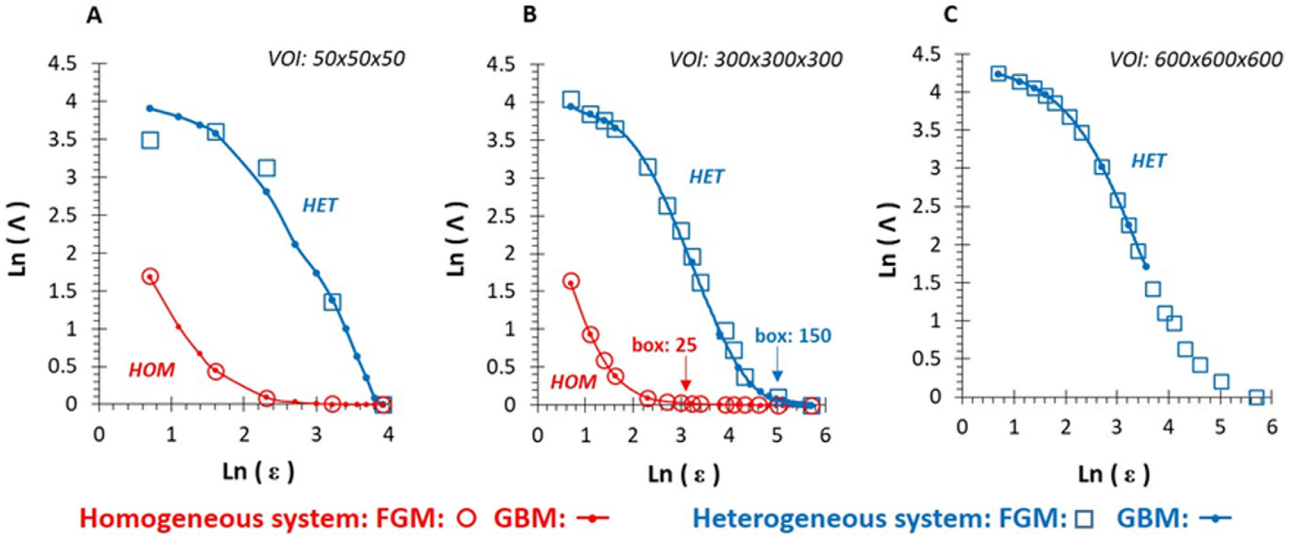

Fig. 7. Comparison of ln(Λ) vs. ln (ε) curves of the rock core samples homogeneously distributed sand grain texture (red) and the concrete cube samples heterogeneously distributed pore texture (blue) at different VOI sizes obtained by gliding box (lines with dots) and fixed-grid (circles and squares, respectively) methods: (A) 50 × 50 × 50, (B) 300 × 300 × 300, (C) 600 × 600 × 600. (For interpretation of the references to color in this figure legend, the reader is referred to the web version of this article.)

geneous structures. With the increase in volume, the dataset becomes more representative of the whole structure at the penalty of drastically increasing computational time. The total computational time for the homogeneous structure with GBM for the M = 300 voxels VOI was 69 h for the full range of box sizes. The total calculation time for a narrower range of box sizes (ε = 2–55) for the same volume size (Fig. 5.D) was 4.4 h, while the same narrow range for an M = 500 voxels volume (Fig. 5.F) was almost 26 h. In contrast, the total computational time with FGM for the full range of boxes of the same volumes was only 10 and 25 s, respectively.

For even larger VOIs (M = 600, 700, and 800) the GBM calculation was only performed for an even narrower range of boxes (ε = 2–35). As shown in Fig. 6 the match between the results obtained by the two methods is excellent (R^2 = 0.999) for this region, which leads to the conclusion that the FGM gives reliable results for the whole range. The total GBM calculation times for M = 800, ε = 2–35 and M = 500, ε = 2–55 were almost the same, ca. 26 h. For the further regions of the lacunarity curves (ε > 35) the FGM provides reliable information relatively fast (t < 1 min), which, compared to the GBM, is negligible.

The shape of the lacunarity curve contains valuable information regarding the heterogeneity of the structures (Fig. 7). For homogeneous textures, the curve is rapidly decreasing, while with increasing heterogeneity the curve flattens. For homogeneous systems, the ln(Λ) value becomes nearly zero at relatively small ε values (ε = 15), whereas for heterogeneous systems this happens at larger box sizes (ε = 150). The heterogeneity of two different patterns can be compared by their ln(Λ) values at the same box sizes, or by the ε values where their lacunarity curve cuts off to ln(Λ) ≈ 0, also show their differences.

3.2. Calculation time

The total calculation time is a cardinal aspect of accurate and detailed lacunarity calculation (see Figs. S3 and S4). Table 3. contains the most important data regarding the calculations for VOIs of M = 100, 200 … 800 voxels. The values of almost every parameter (the number of data points, RAM usage, the number of boxes, and calculation times) rapidly increase with the volume sizes. From the number of boxes and the operations/box the total computa-

Table 3
Comparison of the number of voxels, the RAM usage, the total number of boxes at $\varepsilon = 50$ in case of FGM and GBM methods, the total calculation times for GBM in a narrow range of box sizes (2–55) and FGM in the full range of ε values, and the goodness of fit at different VOI sizes.

			Box 50		Total time 2–55 *	Total time full range	Goodness of fit **
VOI	Points	RAM (MB) ***	FGM	GBM	t (h), GBM	t (s), FGM	R^2
100	1 000 000	105	8	132 651	0.04	1	0.991
200	8 000 000	115	64	3 442 951	1.00	2	0.999
300	27 000 000	140	216	15 813 251	4.48	10	0.998
400	64 000 000	175	512	43 243 551	12.11	17	0.999
500	125 000 000	240	1 000	91 733 851	25.56	25	0.999
600	216 000 000	330	1 728	167 284 151	48.96	32	0.999
700	343 000 000	470	2 744	275 894 451	80.56	41	0.998
800	512 000 000	645	4 096	423 564 751	123.47	47	0.999

* Box size steps: 2,3,4,5,15,25,35,45,55.
** R^2 of the linear curve when plotting GBM datapoints as the function of FGM datapoints.
*** With the memory usage of the calculating software (~ 100 MB) - during the calculations, this can expand to four times the value.

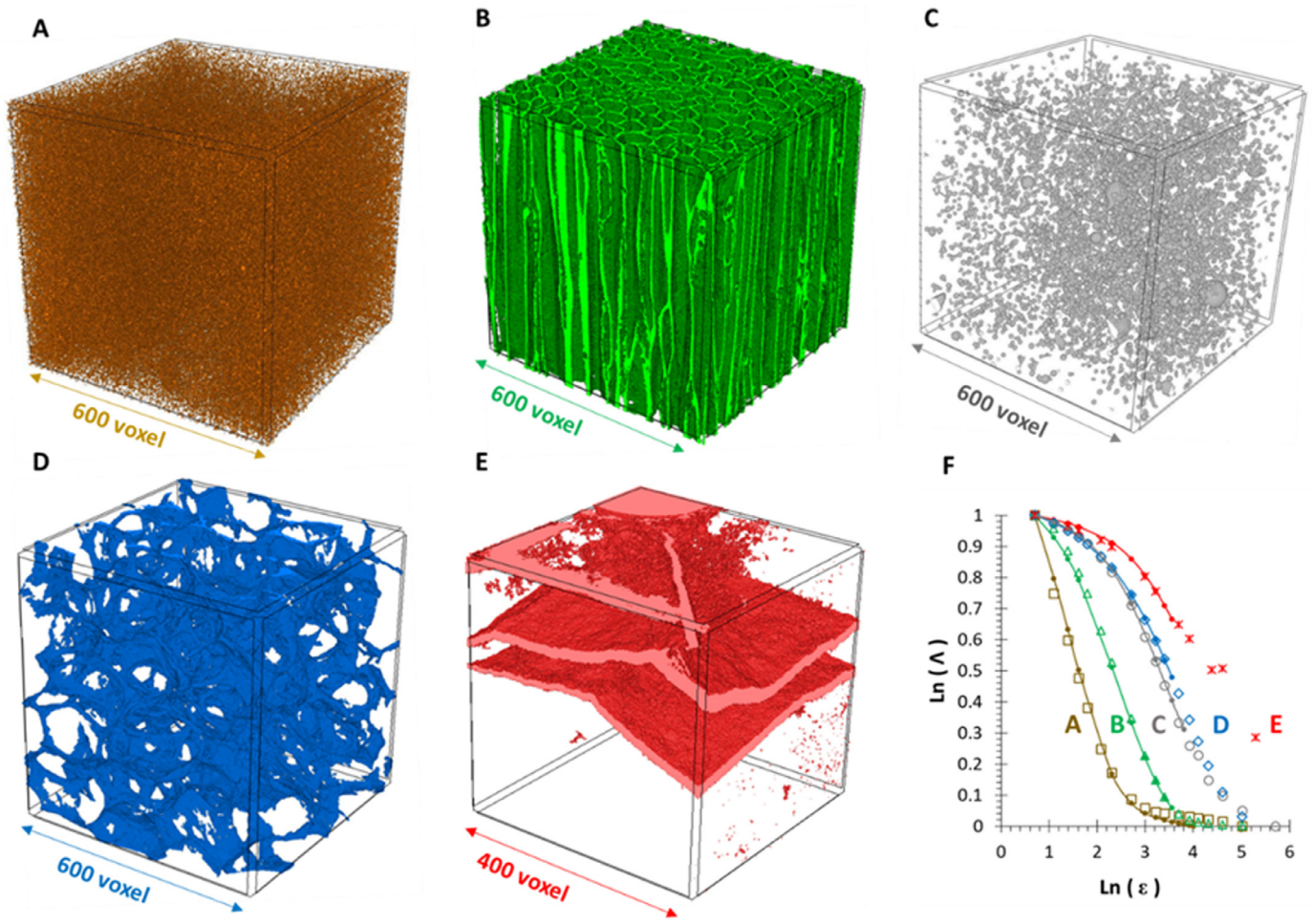

Fig. 8. Representative VOIs from 3D micro-CT datasets of five different samples: A is the pore structure of a limestone sample, B is the ordered fibers of a piece of timber, C is a mortar sample's pore structure, D is the framework of an Al foam and E is the fracture network of an andesite rock sample. F shows the corresponding lacunarity curves calculated by gliding box (solid lines with dots) and fixed-grid (points) methods. (For interpretation of the references to color in this figure legend, the reader is referred to the web version of this article.)

tional time can be calculated for a given range and step size (see in detail in Figs. S5-S7). Table 3. shows calculated values for the total time of GBM (for $\varepsilon = 2$–55), which are in good agreement with the real computational times shown on Fig. 5. It is also visible, that the results of the FGM are in good agreement with the GBM results from $M = 200$ voxels VOI sizes ($R^2 = 0.998$–0.999), while the total calculation time stays under a minute even for an $M = 800$ voxels VOI. These results validate the use of FGM for lacunarity calculations of real micro-CT datasets. Summarizing, we advise using the GBM for small, heterogeneous datasets since the difference in calculation time is not substantial in this case, and using the FGM in all other cases (i.e. small homogeneous datasets and all large datasets).

3.4. Archetypal materials science examples

The applicability of our fixed-grid calculation method for real-life problems was demonstrated by conducting lacunarity calcula-

tions on archetypal material patterns from quasi-homogeneous to heterogeneous. Fig. 8.A-E illustrate the chosen VOIs of five different samples, with VOI sizes ranging from $M = 400$ to 600 voxels: A is the pore structure of a limestone sample, B is the ordered fibers of a piece of timber, C is a mortar sample's pore structure, D is the framework of an Al foam and E is the fracture network of an andesite rock sample. Fig. 8.F shows the corresponding normalized lacunarity curves. Fig. 8.A-E are ordered according to increasing heterogeneity, which is obvious even by simply observing the structures. Nevertheless, the lacunarity function offers an excellent way to quantify the differences: the lacunarity values at $\ln(\varepsilon) = 3.219$ ($\varepsilon = 25$) are $\ln(\Lambda) = 0.058$, 0.149, 0.529, 0.597 and 0.755, respectively. Other than that, the ε values where $\ln(\Lambda)$ becomes nearly zero are good descriptors of the heterogeneity, because they exhibit an increasing trend with the heterogeneity. This approach is applicable if the dataset does not contain hidden patterns, thus the lacunarity curve is a strictly monotonically decreasing one. In Fig. 8.F the result of GBM are represented by solid lines, while the results of FGM are represented by points; it is clearly visible that the values from the two methods are in good agreement with each other. It is important to note that further conclusions regarding the structure or properties of these samples cannot be drawn from these lacunarity curves, since the samples were scanned at different pixel resolutions. This section, however, gives the reader an overview of the appearance of structures with different heterogeneity and a great demonstration of the changes in the shape of the lacunarity curves with changing heterogeneity.

Conclusions

We successfully utilized a fixed-grid method (FGM) to calculate the micro-CT based lacunarity (Λ) curves of several materials and compared the results to the widely used gliding box method (GBM). The greatest advantage of FGM is that it uses fewer boxes for the lacunarity calculations, resulting in a considerably faster calculation. The gain is so significant (from up to hundreds of hours to seconds) that it makes lacunarity calculations feasible on large 3D micro-CT datasets that were previously considered to be computationally inaccessible. The trade-off with FGM is that fewer data points can lead to decreased accuracy. However, we have proven here that while this effect is prominent for small volume of interests, it becomes negligible for large ones. The accuracy increases from an R^2 value of 0.991 to 0.999 with increasing volume size and homogeneity, therefore, FGM can routinely be used for lacunarity calculations for large 3D datasets (cubic volume of interests from an edge length of 200 voxels) with great accuracy and short calculation time. We suggest that lacunarity calculations should be added to the routine micro-CT analysis toolbox. For smaller datasets, the traditional GBM should be used to calculate lacunarity, while for large 3D micro-CT datasets the use of the described FGM is advised. We make the Lac3D software developed for the latter calculation openly available in the electronic Supplementary Information and encourage micro-CT users to utilize the extra information gained from lacunarity in their own projects. Furthermore, fixed-grid lacunarity calculation and Lac3D software are useful not only for the micro-CT community but for all kinds of 3D imaging applications (e.g. FIB-SEM, MRI, confocal microscopy), even beyond materials science.

Author contributions

Conceptualization: Á. Kukovecz, D. Sebők; Methodology: L. Vásárhelyi, D. Sebők; Software: D. Sebők; Writing—original draft preparation: L. Vásárhelyi, D. Sebők, I. Szenti; Writing—review and editing: Á. Kukovecz, R. Vajtai; Supervision: Á. Kukovecz, Z. Kónya, R. Vajtai

Declaration of Competing Interest

The authors declare that they have no known competing financial interests or personal relationships that could have appeared to influence the work reported in this paper.

Acknowledgement

Supported by the ÚNKP-20-5 -SZTE-664 New National Excellence Program of the Ministry for Innovation and Technology from the source of the National Research, Development and Innovation Fund (D.S). The NKFIH GINOP-2.3.3-15-2016-00010 project and the János Bolyai Research Scholarship of the Hungarian Academy of Sciences (D.S.) are acknowledged.

Supplementary materials

Supplementary material associated with this article can be found, in the online version, at doi:10.1016/j.actamat.2021.116970.

References

[1] L. Vásárhelyi, Z. Kónya, Á. Kukovecz, R. Vajtai, Microcomputed tomography–based characterization of advanced materials: a review, Mater. Today Adv. 8 (2020) 100084, doi:10.1016/j.mtadv.2020.100084.
[2] P.J. Withers, C. Bouman, S. Carmignato, V. Cnudde, D. Grimaldi, C.K. Hagen, E. Maire, M. Manley, A. Du Plessis, S.R. Stock, X-ray computed tomography, Nat. Rev. Methods Prim. 1 (2021) 18, doi:10.1038/s43586-021-00015-4.
[3] G.N. Hounsfield, Computerized transverse axial scanning (tomography): part I. Description of system, Br. J. Radiol. 46 (1973) 1016–1022, doi:10.1016/0360-3016(94)E0127-6.
[4] A. Rawal, S. Sharma, D. Singh, N.K. Jangir, H. Saraswat, D. Sebők, A. Kukovecz, D. Hietel, M. Dauner, L. Onal, Out-of-plane auxetic nonwoven as a designer meta-biomaterial, J. Mech. Behav. Biomed. Mater. 112 (2020) 104069, doi:10.1016/j.jmbbm.2020.104069.
[5] D. Takács, G. Schuszter, D. Sebők, Á. Kukovecz, D. Horváth, Á. Tóth, Magnetic-field-manipulated growth of flow-driven precipitate membrane tubes, Chem. – A Eur. J. 25 (2019) 14826–14833, doi:10.1002/chem.201902830.
[6] A. du Plessis, W.P. Boshoff, A review of X-ray computed tomography of concrete and asphalt construction materials, Constr. Build. Mater. 199 (2019) 637–651, doi:10.1016/j.conbuildmat.2018.12.049.
[7] K. Schladitz, Quantitative micro-CT, J. Microsc. 243 (2011) 111–117, doi:10.1111/j.1365-2818.2011.03513.x.
[8] Y. XIA, J. CAI, W. WEI, X. HU, X. WANG, X. GE, A new method for calculating fractal dimensions of porous media based on pore size distribution, Fractals 26 (2018) 1850006, doi:10.1142/S0218348X18500068.
[9] R.D. Peng, Y.C. Yang, Y. Ju, L.T. Mao, Y.M. Yang, Computation of fractal dimension of rock pores based on gray CT images, Chin. Sci. Bull. 56 (2011) 3346–3357, doi:10.1007/s11434-011-4683-9.
[10] B.B. Mandelbrot, The Fractal Geometry of Nature, Freeman, San Francisco, 1982.
[11] J.E. Cutting, J.J. Garvin, Fractal curves and complexity, Percept. Psychophys. 42 (1987) 365–370, doi:10.3758/BF03203093.
[12] N. Sarkar, B.B. Chaudhuri, An efficient differential box-counting approach to compute fractal dimension of image, IEEE Trans. Syst. Man Cybern. 24 (1994) 115–120, doi:10.1109/21.259692.
[13] X. Chen, G. Yao, J. Cai, Y. Huang, X. Yuan, Fractal and multifractal analysis of different hydraulic flow units based on micro-CT images, J. Nat. Gas Sci. Eng. 48 (2017) 145–156, doi:10.1016/j.jngse.2016.11.048.
[14] L. Kong, M. Ostadhassan, X. Hou, M. Mann, C. Li, Microstructure characteristics and fractal analysis of 3D-printed sandstone using micro-CT and SEM-EDS, J. Pet. Sci. Eng. 175 (2019) 1039–1048, doi:10.1016/j.petrol.2019.01.050.
[15] D. Chappard, I.C. Stancu, Porosity imaged by a vector projection algorithm correlates with fractal dimension measured on 3D models obtained by microCT, J. Microsc. 258 (2015) 24–30, doi:10.1111/jmi.12212.
[16] T.G. Smith, G.D. Lange, W.B. Marks, Fractal methods and results in cellular morphology - Dimensions, lacunarity and multifractals, J. Neurosci. Methods. 69 (1996) 123–136, doi:10.1016/S0165-0270(96)00080-5.
[17] R.H.C. de Melo, A. Conci, How Succolarity could be used as another fractal measure in image analysis, Telecommun. Syst. 52 (2013) 1643–1655, doi:10.1007/s11235-011-9657-3.
[18] Y. Gefen, Y. Meir, B.B. Mandelbrot, A. Aharony, Geometric implementation of hypercubic lattices with noninteger dimensionality by use of low lacunarity fractal lattices, Phys. Rev. Lett. 50 (1983) 145–148, doi:10.1103/PhysRevLett.50.145.
[19] M.A. Reiss, B. Lemmerer, A. Hanslmeier, H. Ahammer, Tug-of-war lacunarity—a novel approach for estimating lacunarity, Chaos An Interdiscip. J. Nonlinear Sci. 26 (2016) 113102, doi:10.1063/1.4966539.
[20] S. Gilmore, R. Hofmann-Wellenhof, J. Muir, H.P. Soyer, Lacunarity analysis: a promising method for the automated assessment of melanocytic naevi and melanoma, PLoS ONE 4 (2009) e7449, doi:10.1371/journal.pone.0007449.

[21] C.C. Drăghici, I. Andronache, H. Ahammer, D. Peptenatu, R.D. Pintilii, A.M. Ciobotaru, A.G. Simion, R.C. Dobrea, D.C. Diaconu, M.C. Vișan, R.M. Papuc, Spatial evolution of forest areas in the northern Carpathian mountains of Romania, Acta Montan. Slovaca. 22 (2017) 95–106.
[22] J.E. García-Farieta, R.A. Casas-Miranda, Effect of observational holes in fractal analysis of galaxy survey masks, Chaos, Solit. Fract. 111 (2018) 128–137, doi:10.1016/j.chaos.2018.04.018.
[23] N.A. Valous, D.W. Sun, P. Allen, F. Mendoza, The use of lacunarity for visual texture characterization of pre-sliced cooked pork ham surface intensities, Food Res. Int. 43 (2010) 387–395, doi:10.1016/j.foodres.2009.10.018.
[24] M.V. Nichita, M.A. Paun, V.A. Paun, V.P. Paun, Fractal analysis of brain glial cells. Fractal dimension and lacunarity, UPB Sci. Bull. Ser. A Appl. Math. Phys. 81 (2019) 273–284.
[25] P. Waliszewski, The quantitative criteria based on the fractal dimensions, entropy, and lacunarity for the spatial distribution of cancer cell nuclei enable identification of low or high aggressive prostate carcinomas, Front. Physiol. 7 (2016) 1–16, doi:10.3389/fphys.2016.00034.
[26] B. Sanghera, D. Banerjee, A. Khan, I. Simcock, J.J. Stirling, R. Glynne-Jones, V. Goh, Reproducibility of 2D and 3D fractal analysis techniques for the assessment of spatial heterogeneity of regional blood flow in rectal cancer, Radiology 263 (2012) 865–873, doi:10.1148/radiol.12111316.
[27] O.S. Al-Kadi, D. Watson, Texture analysis of aggressive and nonaggressive lung tumor CE CT images, IEEE Trans. Biomed. Eng. 55 (2008) 1822–1830, doi:10.1109/TBME.2008.919735.
[28] D.A. Palanivel, S. Natarajan, S. Gopalakrishnan, R. Jennane, Multifractal-based lacunarity analysis of trabecular bone in radiography, Comput. Biol. Med. 116 (2020) 103559, doi:10.1016/j.compbiomed.2019.103559.
[29] G. Dougherty, G.M. Henebry, Lacunarity analysis of spatial pattern in CT images of vertebral trabecular bone for assessing osteoporosis, Med. Eng. Phys. 24 (2002) 129–138, doi:10.1016/S1350-4533(01)00106-0.
[30] S.R. Majumder, S. Mazumdar, Mechanical breakdown of trabecular bone: dependence on microstructure, Phys. A Stat. Mech. Its Appl. 377 (2007) 559–564, doi:10.1016/j.physa.2006.11.069.
[31] S.R. Majumder, T. Bandyopadhyay, S.K. Ghosh, Mechanical stability of end-linked polymer gel, Radiat. Phys. Chem. 74 (2005) 252–260, doi:10.1016/j.radphyschem.2005.04.018.
[32] R.A. Dorey, J.A. Yeomans, P.A. Smith, Effect of pore clustering on the mechanical properties of ceramics, J. Eur. Ceram. Soc. 22 (2002) 403–409, doi:10.1016/S0955-2219(01)00303-X.
[33] I. Netinger Grubeša, B. Marković, M. Vračević, M. Tunkiewicz, I. Szenti, Á. Kukovecz, Pore structure as a response to the freeze/thaw resistance of mortars, Materials (Basel) 12 (2019) 3196, doi:10.3390/ma12193196.
[34] I. Netinger Grubeša, M. Vračević, V. Ducman, B. Marković, I. Szenti, Á. Kukovecz, Influence of the size and type of pores on brick resistance to freeze-thaw cycles, Materials (Basel) 13 (2020) 3717, doi:10.3390/ma13173717.
[35] Y. Liu, D.S. Jeng, Pore structure of grain-size fractal granular material, Materials (Basel) 12 (2019) 1–26, doi:10.3390/ma12132053.
[36] C.R. Dos Santos, A.C.D. Antonino, R.J. Heck, L.R.R. de Lucena, A.C.H. de Oliveira, A.S.A. da Silva, B. Stosic, R.S.C. Menezes, 3D soil void space lacunarity as an index of degradation after land use change, Acta Sci. - Agron. 42 (2020) 1–9, doi:10.4025/actasciagron.v42i1.42941.
[37] K. Liu, M. Ostadhassan, Quantification of the microstructures of Bakken shale reservoirs using multi-fractal and lacunarity analysis, J. Nat. Gas Sci. Eng. 39 (2017) 62–71, doi:10.1016/j.jngse.2017.01.035.
[38] Y. Xia, J. Cai, E. Perfect, W. Wei, Q. Zhang, Q. Meng, Fractal dimension, lacunarity and succolarity analyses on CT images of reservoir rocks for permeability prediction, J. Hydrol. 579 (2019) 124198, doi:10.1016/j.jhydrol.2019.124198.
[39] M. N'Diaye, C. Degeratu, J.M. Bouler, D. Chappard, Biomaterial porosity determined by fractal dimensions, succolarity and lacunarity on microcomputed tomographic images, Mater. Sci. Eng. C. 33 (2013) 2025–2030, doi:10.1016/j.msec.2013.01.020.
[40] D. Massai, F. Pennella, P. Gentile, D. Gallo, G. Ciardelli, C. Bignardi, A. Audenino, U. Morbiducci, Image-based three-dimensional analysis to characterize the texture of porous scaffolds, Biomed Res. Int. 2014 (2014) 1–8, doi:10.1155/2014/161437.
[41] R. Smajda, Á. Kukovecz, Z. Kónya, I. Kiricsi, Structure and gas permeability of multi-wall carbon nanotube buckypapers, Carbon N. Y. 45 (2007) 1176–1184, doi:10.1016/j.carbon.2007.02.022.
[42] A. Pander, T. Onishi, A. Hatta, H. Furuta, Study of self-organized structure in carbon nanotube forest by fractal dimension and lacunarity analysis, Mater. Charact. 160 (2020) 110086, doi:10.1016/j.matchar.2019.110086.
[43] F. Imani, B. Yao, R. Chen, P. Rao, H. Yang, Joint multifractal and lacunarity analysis of image profiles for manufacturing quality control, J. Manuf. Sci. Eng. (2019) 141, doi:10.1115/1.4042579.
[44] A. Carpinteri, B. Chiaia, S. Invernizzi, Three-dimensional fractal analysis of concrete fracture at the meso-level, Theor. Appl. Fract. Mech. 31 (1999) 163–172, doi:10.1016/S0167-8442(99)00011-7.
[45] A. Carpinteri, B. Chiaia, S. Invernizzi, Three-dimensional fractal analysis of microstructural morphologies in concrete, Fract. Mech. Concr. Struct. 3 (1994) 281–292.
[46] F. Pennella, M. Rossi, S. Ripandelli, M. Rasponi, F. Mastrangelo, M.A. Deriu, L. Ridolfi, C.J. Kähler, U. Morbiducci, Numerical and experimental characterization of a novel modular passive micromixer, Biomed. Microdevices. 14 (2012) 849–862, doi:10.1007/s10544-012-9665-4.
[47] R.E. Plotnick, R.H. Gardner, W.W. Hargrove, K. Prestegaard, M. Perlmutter, Lacunarity analysis: a general technique for the analysis of spatial patterns, Phys. Rev. E. 53 (1996) 5461–5468, doi:10.1103/PhysRevE.53.5461.
[48] A. Roy, E. Perfect, W.M. Dunne, L.D. McKay, A technique for revealing scale-dependent patterns in fracture spacing data, J. Geophys. Res. Solid Earth. 119 (2014) 5979–5986, doi:10.1002/2013JB010647.
[49] C. Allain, M. Cloitre, Characterizing the lacunarity of random and deterministic fractal sets, Phys. Rev. A. 44 (1991) 3552–3558, doi:10.1103/PhysRevA.44.3552.
[50] A. Hanen, B. Imen, B.A. Asma, D. Patrick, B.M. Hédi, Multifractal modelling and 3D lacunarity analysis, Phys. Lett. Sect. A Gen. At. Solid State Phys. 373 (2009) 3604–3609, doi:10.1016/j.physleta.2009.07.087.
[51] C.R. Tolle, T.R. McJunkin, D.T. Rohrbaugh, R.A. LaViolette, Lacunarity definition for ramified data sets based on optimal cover, Phys. D Nonlinear Phenom. 179 (2003) 129–152, doi:10.1016/S0167-2789(03)00029-0.
[52] C.R. Tolle, T.R. McJunkin, D.J. Gorsich, An efficient implementation of the gliding box lacunarity algorithm, Phys. D Nonlinear Phenom. 237 (2008) 306–315, doi:10.1016/j.physd.2007.09.017.
[53] A.R. Backes, A new approach to estimate lacunarity of texture images, Pattern Recognit. Lett. 34 (2013) 1455–1461, doi:10.1016/j.patrec.2013.05.008.
[54] A. Karperien, FracLac for ImageJ, 2014, doi:10.13140/2.1.4775.8402.
[55] R.E. Plotnick, R.H. Gardner, R.V. O'Neill, Lacunarity indices as measures of landscape texture, Landsc. Ecol. 8 (1993) 201–211, doi:10.1007/BF00125351.
[56] Free Pascal Team, Free Pascal: A 32, 64 and 16 Bit Professional Pascal compiler. Version 3.0.4, 1993-2019) URL https://www.freepascal.org. RRID: SCR_014360.
[57] Lazarus Team, Lazarus: The professional Free Pascal RAD IDE. Version 1.8.4, 1993–2019 URL http://www.lazarus-ide.org. RRID: SCR_014362.